Multicloud Models for Organized Tropical Convection: Enhanced Congestus Heating

BOUALEM KHOUIDER

Department of Mathematics and Statistics, University of Victoria, Victoria, British Columbia, Canada

ANDREW J. MAJDA

Department of Mathematics, and Center for Atmosphere/Ocean Sciences, Courant Institute, New York University, New York, New York

(Manuscript received 23 January 2007, in final form 17 May 2007)

ABSTRACT

Despite the recent advances in supercomputing, the current general circulation models (GCMs) poorly represent the large-scale variability associated with tropical convection. Multicloud model convective parameterizations based on three cloud types (congestus, deep, and stratiform), introduced recently by the authors, have been revealed to be very useful in representing key features of organized convection and convectively coupled waves. Here a new systematic version of the multicloud models is developed with separate upper- and lower-troposphere basis functions for the congestus and stratiform clouds. It naturally leads to a new convective closure for the multicloud models enhancing the congestus heating in order to better pinpoint the congestus preconditioning and moistening mechanisms. The models are studied here for flows above the equator without rotation effects. First, the new model results consist of the usual synoptic-scale convectively coupled moist gravity wave packets moving at 15–20 m s^{-1} but, in addition, these packets have planetary-scale envelopes moving in the opposite direction at about 6 m s^{-1} and have many of the self-similar features of convectively coupled waves, reminiscent of the Madden–Julian oscillation. Second, when a warm pool forcing is imposed, dry regions of roughly 250 km in extent form "convective barriers" surrounding the warm pool region where only congestus heating survives. Deep convection and moist gravity waves are thus confined within the warm pool region. Finally, linear analysis reveals that, for sufficiently dry mean states, in addition to the inherent synoptic-scale moist gravity waves, the new model supports a planetary (wavenumber 1) standing congestus mode that provides, within its congestus active phase, a region where moist gravity waves evolve and propagate, which results in a Walker-like circulation over a uniform SST background.

1. Introduction

Organized convection in the tropics involves a hierarchy of scales ranging from hundreds of kilometers owing to mesoscale organized squall lines to intraseasonal oscillations over planetary scales on the order of 40 000 km (Nakazawa 1988; Hendon and Liebmann 1994; Wheeler and Kiladis 1999). Despite the recent advances in supercomputing, the present general circulation models (GCMs) used for the prediction of weather and climate at best represent the large-scale variability associated with tropical convection poorly (Slingo et al. 1996; Moncrieff and Klinker 1997; Scinocca and McFarlane 2004; Lau and Waliser 2005; Zhang 2005; Lin et al. 2006). In GCMs, the physical equations representing these extremely complex flows are discretized in space and time, and the effects of unresolved processes are parameterized according to various recipes (Emanuel and Raymond 1993; Smith 1997). Given the importance of the tropics for short-term climate, the search for new strategies for parameterizing the unresolved effects of tropical convection, and in particular, for new theoretical models for the tropical intraseasonal oscillation, known as the Madden–Julian oscillation (MJO), the dominant component of tropical intraseasonal variability (Lau and Waliser 2005; Zhang 2005), has been the focus of researchers in the field during the last few decades.

Apparently, the reduced tropical variability in GCMs

Corresponding author address: Dr. Boualem Khouider, Department of Mathematics and Statistics, University of Victoria, P.O. Box 3045, STN CSC, Victoria, BC V8W 3P4, Canada.
E-mail: khouider@math.uvic.ca

DOI: 10.1175/2007JAS2408.1

© 2008 American Meteorological Society

is due to a poor representation of observed large-scale tropical disturbances associated with organized tropical convection, such as convectively coupled waves and the related planetary-scale tropical circulation (Slingo et al. 1996; Moncrieff and Klinker 1997; Lin et al. 2006); the reasons for such poor performance are not well understood. An adequate representation of the interactions across temporal and spatial scales between the large-scale circulation and organized cloud systems, from individual clouds to large-scale clusters and superclusters to planetary-scale disturbances, is one of the major challenges facing the atmospheric community.

Simplified models with crude vertical resolution, typically involving one or two baroclinic vertical modes, are commonly used for theoretical and numerical studies of various strategies for parameterizing moist convection and convectively coupled waves (Emanuel 1987; Mapes 1993; Neelin and Yu 1994; Yano et al. 1995, 1998; Mapes 2000; Neelin and Zeng 2000; Majda and Shefter 2001a,b; Raymond 2001; Fuchs and Raymond 2002; Majda and Khouider 2002; Majda et al. 2004, 2007; Khouider and Majda 2006a, hereafter KM06; Khouider and Majda 2006b,c, 2007).

Recent analysis of convectively coupled waves on large scales reveals a multicloud convective structure with leading shallow congestus cloud decks that moisten and precondition the lower troposphere, followed by deep convection, and finally trailing decks of stratiform precipitation; this structure applies to the eastward propagating convectively coupled Kelvin waves (Wheeler and Kiladis 1999; Wheeler et al. 2000; Straub and Kiladis 2002) and westward propagating two-day waves (Haertl and Kiladis 2004), which reside on equatorial synoptic scales on the order of 1000–3000 km in the lower troposphere, as well as the planetary-scale MJO (Dunkerton and Crum 1995; Kiladis et al. 2005). An inherently multiscale theory for the Madden–Julian oscillation, with qualitative agreement with observations, based on these three cloud types, has been developed by Majda and Biello (2004) and Biello and Majda (2005) when the phase of this wave is prescribed. A more recent study based on systematic multiscale asymptotic theory explores the systematic self-similarity in convectively coupled tropical waves from mesoscale squall lines to synoptic-scale superclusters to the intraseasonal and planetary disturbances from the perspective of simplified multiscale models (Majda 2007).

Multicloud model convective parameterizations based on these three cloud types were introduced by KM06 (see also Khouider and Majda 2006b,c, 2007; Majda et al. 2007). In these works the multicloud models were studied and analyzed using both linear and nonlinear simulations around the equator in the case without rotation. It is found that these models have intrinsic moist gravity waves that are unstable at the synoptic scales and move at roughly 15–20 m s^{-1}, with dynamical features resembling those of convectively coupled Kelvin waves observed in the tropics. More importantly, these new models demonstrated the role of congestus heating in the lower troposphere and the induced low-level moisture convergence that helps the moistening and preconditioning of the tropical troposphere prior to deep convection. Furthermore, the nonlinear simulations reported by the authors in a prototype Walker-cell environment (Khouider and Majda 2007) revealed moist gravity wave packets with 15–20 m s^{-1} phase speed, as predicted by linear theory, and convective envelopes over the warm pool, which often move in the opposite direction at speeds ranging from 2 to 5 m s^{-1}.

Here the basic multicloud models (KM06) are generalized with a local vertical basis in (2.1) to allow for asymmetric local heating and cooling in congestus and stratiform heating fields. This has the important practical consequence that there are significant contributions from stratiform and congestus clouds to the precipitation budget. Within this new framework, an enhanced congestus parameterization is proposed here. The main idea exploited here is that congestus clouds respond to a convective instability much like deep convective clouds with the exception that they do not penetrate deeper than the melting level. Congestus heating is therefore tied to an adjustment process toward a linearized CAPE-like closure. As in KM06, a moisture switch distributes available energy for convection onto deep and/or congestus heating according to whether the atmosphere is moist or dry. This closure is developed through conservation of vertically integrated moist static energy as a design principle.

The rest of the paper is organized as follows. After stating the motivation and introducing the basis functions associated with the three cloud types, the multicloud model parameterization with the new congestus closure is presented in section 2. In section 3, we present a linear stability analysis around a radiative convective equilibrium (RCE) solution. We emphasize the emergence of a standing congestus mode that is unstable at wavenumber 1 as the RCE transits from a deep-convective-dominated to a congestus-dominated regime. Section 4 is devoted to nonlinear simulations. First, we consider the deep-convective-dominated regime with and without a warm-pool sea surface temperature (SST) gradient, and then consider the case

when the congestus heating at RCE and the growth of the planetary standing mode dominate. We finally conclude this paper by a brief discussion in section 5.

2. The multicloud convective models with enhanced congestus heating

a. Cloud forcing and the vertical basis functions

Recent observations of organized tropical convection (Lin and Johnson 1996; Johnson et al. 1999; Mapes et al. 2006) point to three cloud types. Emanating at their cloud base near the top of the well-mixed planetary boundary layer, convective clouds in the tropics can be divided as follows. On the one hand we have nonprecipitating shallow cumulus clouds, topped by the trade wind inversion layer, and on the other hand we have precipitating cumulus comprising congestus clouds, with tops near the 0°C layer at the middle of the troposphere, cumulonimbus (deep convective) clouds, with tops near the tropopause (Lin and Johnson 1996; Johnson et al. 1999), and stratiform anvil clouds, evolving within the upper half of the troposphere, in the wake of deep convection (Mapes 2000). These last three cloud types are believed to be responsible for the bulk of tropical rainfall and constitute the major source of heat for the free-tropospheric circulation:

1) Cumulus congestus heat the lower troposphere, through latent heat release associated with condensation and precipitation, and cool the middle and upper troposphere, through detrainment at cloud tops near the 0°C melting layer as well as the high reflectivity associated with their icy cloud tops. The precipitation from congestus clouds represents a moisture sink within the lower troposphere, but overall we believe that congestus clouds serve to moisten and precondition the middle troposphere prior to deep convection so that convective parcels can reach and pass the freezing level and enhance their buoyancy.
2) Deep convective cumulonimbus clouds warm and dry the entire tropospheric depth and produce the majority of tropical rainfall.
3) Stratiform clouds warm and dry the upper troposphere by stratiform convection and precipitation and cool and moisten the lower troposphere by the evaporation of stratiform rain within the relatively warm and dry lower troposphere (after the passage of deep convection).

The dynamical interactions between the three cloud types and the tropical boundary layer, above the sea surface, are sketched in Fig. 1a. The new multicloud models assume the following idealized vertical profiles for the convective heating and cooling fields associated with the three cloud types:

$$
\begin{aligned}
C_d(x, y, z, t) &= H_d(x, y, t)\Phi_1(z),\\
C_s(x, y, z, t) &= H_s(x, y, t)\Phi_2(Z_T - z),\\
E_s(x, y, z, t) &= -\delta_s H_s(x, y, t)\Phi_2(z),\\
C_c(x, y, z, t) &= H_c(x, y, t)\Phi_2(z),\\
E_c(x, y, z, t) &= -\delta_c H_c(x, y, t)\Phi_2(Z_T - z), \qquad (2.1)
\end{aligned}
$$

where C_d, C_c, and C_s are the convective heating rates associated with deep, congestus, and stratiform clouds, respectively, while E_s and E_c are the cooling rates associated with the evaporation of stratiform rain in the lower troposphere and congestus cooling in the upper troposphere, respectively. In (2.1), Φ_1 and Φ_2 are the heating basis functions shown in Fig. 1b with explicit formulas: $\Phi_1(z) = \sqrt{2}\sin(\pi z/Z_T)$, $0 \le z \le Z_T$, and $\Phi_2(z) = \sqrt{2}\sin(2\pi z/Z_T)$, if $0 \le z \le Z_T/2$; $\Phi_2(z) = 0$, if $Z_T/2 \le z \le Z_T$, where $Z_T = 16$ km is the height of the troposphere. The parameters δ_s, δ_c with $0 < \delta_c$, $\delta_s \le 1$ represent, respectively, the fractions of cooling in the upper/lower troposphere over heating in the lower/upper troposphere associated with congestus/stratiform clouds. As shown below, these parameters are related to the fractions of precipitation reaching the ground resulting from congestus and stratiform clouds, respectively. Notice that $\delta_s = \delta_c = 1$ corresponds to the extreme case, where the lower troposphere heating/cooling exactly balances the upper troposphere cooling/heating associated with congestus/stratiform clouds, considered in the original multicloud models (KM06; Khouider and Majda 2006b,c, 2007; Majda et al. 2007).

b. The governing equations

The dynamical equations for the multicloud models are based on the linear equatorial beta-plane primitive equations, forced by the convective heating fields in (2.1), Galerkin projected, accordingly, into the first two baroclinic modes of vertical structure (Majda and Shefter 2001b; Majda et al. 2004; KM06). In the simple case where the beta effect and meridional dependence are ignored, this results in two (forced and coupled) shallow-water systems for the zonal velocity and potential temperature components, u_j, θ_j, $j = 1, 2$, respectively, augmented by an equation for the vertically averaged moisture q and another equation for the boundary layer equivalent potential temperature θ_{eb},

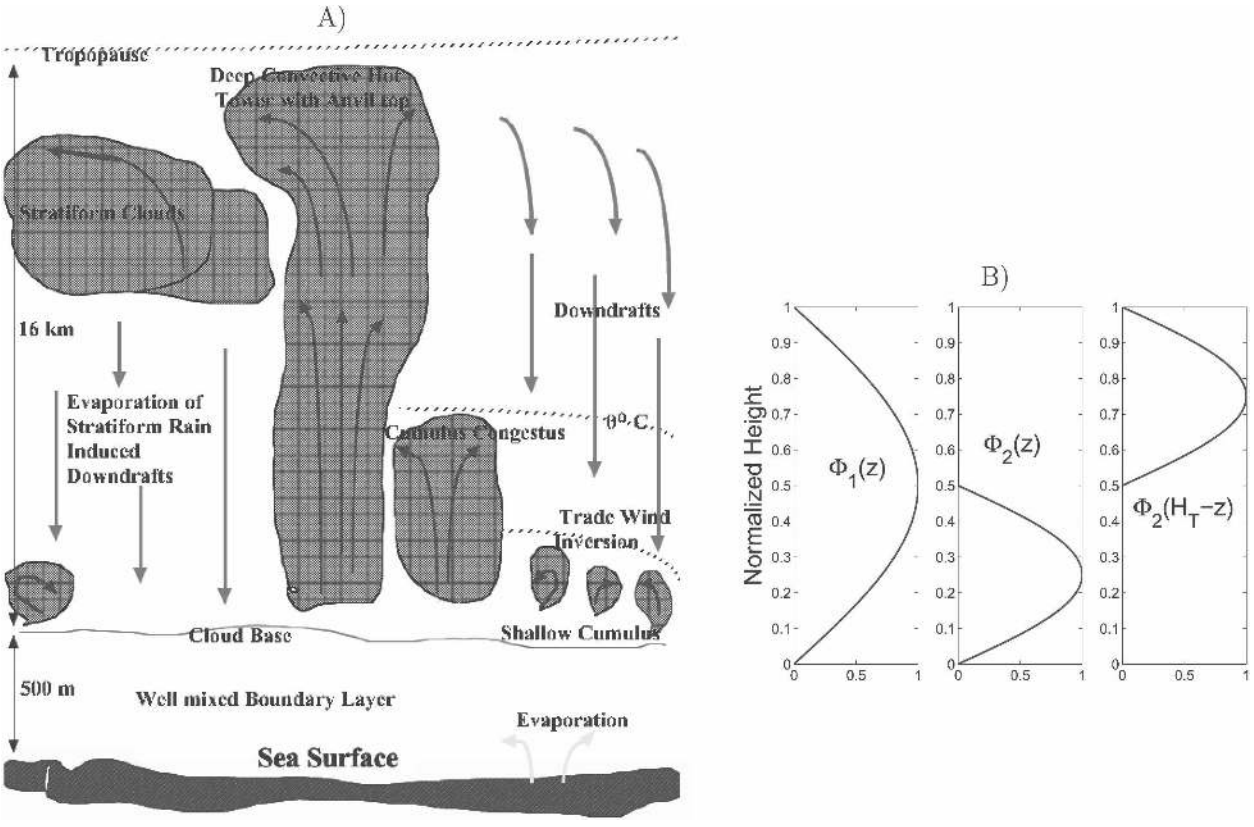

FIG. 1. (a) Schematic of the three tropical cloud types interacting with the well-mixed planetary boundary layer above the sea surface through convective updrafts and downdrafts: the trade wind inversion, 0°C, and tropopause layers are shown. (b) Vertical profile basis functions of heating fields associated with the three cloud types.

$$\begin{cases} \dfrac{\partial u_1}{\partial t} - \dfrac{\partial \theta_1}{\partial x} = -C_d^0 u_0 u_1 - \dfrac{1}{\tau_R} u_1 \\ \dfrac{\partial \theta_1}{\partial t} - \dfrac{\partial u_1}{\partial x} = H_d + \xi_s H_s + \xi_c H_c - Q_{R,1}^0 - \dfrac{1}{\tau_D} \theta_1 \\ \dfrac{\partial u_2}{\partial t} - \dfrac{\partial \theta_2}{\partial x} = -C_d^0 u_0 u_2 - \dfrac{1}{\tau_R} u_2 \\ \dfrac{\partial \theta_2}{\partial t} - \dfrac{1}{4}\dfrac{\partial u_2}{\partial x} = -H_s + H_c - Q_{R,2}^0 - \dfrac{1}{\tau_D} \theta_2, \end{cases} \tag{2.2}$$

$$\frac{\partial q}{\partial t} + \frac{\partial}{\partial x}(u_1 q + \tilde{\alpha} u_2 q) + \tilde{Q}\frac{\partial}{\partial x}(u_1 + \tilde{\lambda} v_2) = -P + E_f, \tag{2.3}$$

$$\frac{\partial \theta_{eb}}{\partial t} = \frac{1}{\tau_e}(\theta_{eb}^* - \theta_{eb}) - \frac{1}{Z_b} D. \tag{2.4}$$

A more thorough and detailed discussion on the model equations in (2.2)–(2.4) is found in (KM06). Nevertheless, a comprehensive list of the model constants and parameters is given in Table 1 for the sake of completeness. Induced by the asymmetric heating profiles in (2.1), the novelty here resides in the contributions of stratiform and congestus clouds to the heating of the first mode. For convenience we set

$$\xi_s = \frac{16}{3\pi}\frac{1 - \delta_s}{1 + \delta_s}$$

and

$$\xi_c = \frac{16}{3\pi}\frac{1 - \delta_c}{1 + \delta_c}.$$

Moreover, we recall that P and E_f in (2.3) are, respectively, the bulk precipitation and free-troposphere evaporation rates representing sinks and sources of moisture. The term

$$\frac{1}{\tau_e}(\theta_{eb}^* - \theta_{eb})$$

in (2.4) is the evaporation at the sea surface, while D represents the environmental and convective downdrafts (see Fig. 1a) that cool and dry the boundary layer after a deep convective episode. Note that θ_{eb}^*, the saturation equivalent potential temperature in the bound-

TABLE 1. Constants and parameters in the multicloud models with enhanced congestus.

Parameter	Typical value utilized	Description
Z_T	16 km	Height of the troposphere
h_b	500 m	Height of the boundary layer
C_d^0	0.001	Momentum drag coefficient
u_0	2 m s^{-1}	Strength of turbulent fluctuations
τ_R	75 days	Rayleigh wind relaxation time scale
τ_D	50 days	Newtonian cooling time scale
$\tilde{\alpha}$	0.1	Coefficient of $\mathbf{v}_2$ in nonlinear moisture convergence term
$\tilde{\lambda}$	0.8	Coefficient of $\mathbf{v}_2$ in linear moisture convergence term
$\tilde{Q}$	0.9	Background moisture stratification
Λ^*	0	Lower threshold of moisture switch
$\theta^{\pm}$	20, 10 K	Moisture switch threshold values
α_s	0.25	Stratiform adjustment coefficient
α_c	0.1	Congestus adjustment coefficient
τ_s	3 h	Stratiform adjustment time scale
τ_{conv}	2 h	Convective time scale
τ_{cong}	$\equiv\tau_{\text{conv}}/\alpha_c$ = 20 h	Congestus heating time scale
τ_c	1 h	Congestus adjustment time scale
τ_e	Determined at RCE	Evaporative time scale in the boundary layer
m_0	Determined at RCE	Downdraft mass flux reference scale
$\theta_{eb}^* - \overline{\theta}_{eb}$	10 K	Discrepancy between boundary layer θ_e at RCE and its saturated value
$\overline{\theta}_{eb} - \overline{\theta}_{em}$	Varies between 11 and 19 K	Discrepancy between boundary layer and middle-troposphere θ_es at RCE
$Q_{R,1}^0$	1 K day^{-1}	Imposed first baroclinic radiative cooling rate
$Q_{R,2}^0$	Determined at RCE	Second baroclinic radiative cooling rate
$\overline{Q}$	Determined at RCE by Eq. (2.11)	Bulk convective heating at RCE
a_1, a_2	0.5	Relative contribution fractions of θ_{eb} and moisture q to deep convection
a_0	5	Coefficient of θ_1 in Q_c formula: inverse convective buoyancy time scale associated with deep clouds
a_0'	2	Coefficient of θ_1 in Q_d formula: inverse convective buoyancy time scale associated with congestus clouds
γ_2	0.1	Relative contribution of θ_2 to deep and congestus bulk heating
α_2	0.1	Relative contribution of θ_2 to θ_{em}
μ	0.25	Relative contribution of stratiform and congestus heating rates to downdrafts
ξ_s	0.5	Relative contribution of stratiform clouds to first baroclinic heating
ξ_c	1.25	Relative contribution of congestus clouds to first baroclinic heating

ary layer, is a function of the SST alone, according to the Clausius–Clapeyron equation. Under the constraint of conservation of vertically averaged moist static energy, the moisture sink and source satisfy

$$P = \frac{2\sqrt{2}}{\pi}(H_d + \xi_s H_s + \xi_c H_c); \quad E_f = \frac{1}{Z_T} D. \tag{2.5}$$

Up to this point, when $\delta_s = \delta_c = 1$, the present formulation remains identical to the original multicloud models, as introduced in KM06 and Khouider and Majda (2006b,c,2007). The modifications leading to the new convective parameterization with an enhanced congestus heating are introduced next.

c. The new congestus parameterization

Recall that one crucial feature of the multicloud models (KM06) is the use of a nonnegative moisture switch function $\Lambda = \Lambda(\theta_{eb} - \theta_{em})$, where

$$\theta_{em} = q + \frac{2\sqrt{2}}{\pi}(\theta_1 + \alpha_2\theta_2)$$

is the equivalent potential temperature in the middle of the troposphere: $\Lambda = 1$, if $\theta_{eb} - \theta_{em} > \theta^+ = 20$ K, $\Lambda = \Lambda_* < 1$, if $\theta_{eb} - \theta_{em} < \theta^- = 10$ K and is linearly continuous in between. In addition to the "bulk energy available for deep convection"

$$Q_d = \left\{\overline{Q} + \frac{1}{\tau_{\text{conv}}}[a_1\theta_{eb} + a_2 q - a_0(\theta_1 + \gamma_2\theta_2)]\right\}^+, \tag{2.6}$$

the new convective closure introduces a "bulk energy" for congestus heating

$$Q_c = \left\{\overline{Q} + \frac{1}{\tau_{\text{conv}}}[\theta_{eb} - a_0'(\theta_1 + \gamma_2\theta_2)]\right\}^+, \tag{2.7}$$

so that

$$H_d = \frac{1-\Lambda}{1-\Lambda^*} Q_d,$$

$$\frac{\partial H_s}{\partial t} = \frac{1}{\tau_s}(\alpha_s H_d - H_s),$$

$$\frac{\partial H_c}{\partial t} = \frac{1}{\tau_c}\left(\alpha_c \frac{\Lambda-\Lambda^*}{1-\Lambda^*} Q_c - H_c\right). \quad (2.8)$$

Recall that in the original multicloud models in KM06, the congestus heating H_c is relaxed toward a fraction of the downdrafts D instead. Except for the moisture switch coefficient, the congestus closure in (2.7) is related to a linearized version of the CAPE adjustment closure introduced earlier for deep convective parameterization in Yano et al. (1998) and Majda and Shefter (2001b), with one important difference: whenever the troposphere is dry but the CAPE is large, congestus clouds develop, as explained in detail next. Note that the same background value is used in the bulk heating equations (2.6) and (2.7) so that at RCE we have $\overline{Q}_c = \overline{Q}_d \equiv \overline{Q}$. Throughout the paper $\overline{X}$ represents the RCE value of the variable X. The dryness/moistness of the troposphere alone determines how much of the bulk convective energy at RCE is distributed between deep and congestus heatings according to the coefficients $1 - \Lambda$ and $\Lambda - \Lambda_*$. The adjustment coefficient α_c yields a congestus time scale $\tau_{\text{cong}} = \tau_{\text{conv}}/\alpha_c$. Note that the values used here of $\alpha_c = 0.1$ and $\tau_{\text{conv}} = 2$ h yield $\tau_{\text{cong}} \approx 1$ day.

Finally, we use a simplified downdraft equation:

$$D = \frac{m_0}{\overline{Q}}[\overline{Q} + \mu(H_s - H_c)]^+(\theta_{eb} - \theta_{em}). \quad (2.9)$$

Unlike KM06, the factor Λ in front is ignored here for simplicity, and as a consequence the threshold $\Lambda^* = 0$ is used instead. Also, because of the enhanced congestus heating a smaller value, $\mu = 0.25$ is used in (2.9).

d. Bulk behavior at RCE

Recall (KM06) that an RCE solution is completely determined if the values of $Q^0_{R,1}$, $\theta^*_{eb} - \overline{\theta}_{eb}$, and $\overline{\theta}_{eb} - \overline{\theta}_{em}$ are prescribed. Here, in particular, we have

$$\overline{H}_d = \frac{1-\overline{\Lambda}}{1-\Lambda^*}\overline{Q}, \quad \overline{H}_c = \alpha_c \frac{\overline{\Lambda}-\Lambda^*}{1-\Lambda^*}\overline{Q}, \quad \text{and}$$

$$\overline{H}_s = \alpha_s \frac{1-\overline{\Lambda}}{1-\Lambda^*}\overline{Q}. \quad (2.10)$$

At RCE with $\overline{\theta}_1 = \overline{\theta}_2 = 0$, we have $\overline{H}_d + \xi_s \overline{H}_s + \xi_c \overline{H}_c = Q^0_{R,1}$, which with (2.10) yields

$$\overline{Q}\left[\frac{1-\overline{\Lambda}}{1-\Lambda^*}(1 + \xi_s\alpha_s) + \xi_c\alpha_c\frac{\overline{\Lambda}-\Lambda^*}{1-\Lambda^*}\right] = Q^0_{R,1}. \quad (2.11)$$

In particular, a purely congestus RCE with $\overline{\Lambda} = 1$ requires $\xi_c\alpha_c\overline{Q} = Q^0_{R,1}$. Such an RCE is only possible when $\xi_c > 0$ ($\delta_c < 1$), that is, when there is a net vertically integrated congestus heating to balance an imposed nontrivial radiative cooling.

According to (2.10), for a given RCE value $\overline{\Lambda}$, the coefficients

$$\frac{1-\overline{\Lambda}}{1-\Lambda^*}, \quad \xi_s\alpha_s\frac{1-\overline{\Lambda}}{1-\Lambda^*}, \quad \text{and} \quad \xi_c\alpha_c\frac{\overline{\Lambda}-\Lambda^*}{1-\Lambda^*}$$

represent, respectively, the actual fractions of precipitation contributed from deep, stratiform, and congestus clouds. Since Λ is allowed to vary, universal fractions independent of $\overline{\Lambda}$ are obtained by averaging over all possible Λ values within the interval $[\Lambda^*, 1]$. By invoking the mean value theorem, we obtain

$$Q^0_{R,1} = \frac{1 + \xi_s\alpha_s + \alpha_c\xi_c}{2}\overline{Q}_m.$$

The averaged fractions of deep convective, stratiform, and congestus precipitation are then given by

$$f_d = \frac{1}{1 + \xi_s\alpha_s + \xi_c\alpha_c}, \quad f_s = \frac{\xi_s\alpha_s}{1 + \xi_s\alpha_s + \xi_c\alpha_c}, \quad \text{and}$$

$$f_c = \frac{\xi_c\alpha_c}{1 + \xi_s\alpha_s + \xi_c\alpha_c}, \quad (2.12)$$

respectively. Notice that, with α_s and α_c given, these fractions allow us to determine the coefficients ξ_s and ξ_c, and vice versa. If, for example, $\alpha_s = 0.25$ and $\alpha_c = 0.1$, as listed in Table 1, the values $f_d = 0.8$, $f_s = f_c = 0.1$, yield $\xi_s = 0.5$, $\xi_c = 1.25$, which are used here.

3. Linear waves and instabilities

In this section we report some typical results of linear stability analysis for the multicloud models with the enhanced congestus closure presented above. We consider linear plane waves about an RCE solution for Eqs. (2.2)–(2.9). This results in an eigenvalue problem for which the real and imaginary parts of a given eigenvalue yield the phase and growth rate for the associated mode (KM06).

a. The three typical unstable waves

Here we summarize the linear theory results for the typical parameter values in Table 1. The sensitivity of these results to parameter variations is discussed briefly

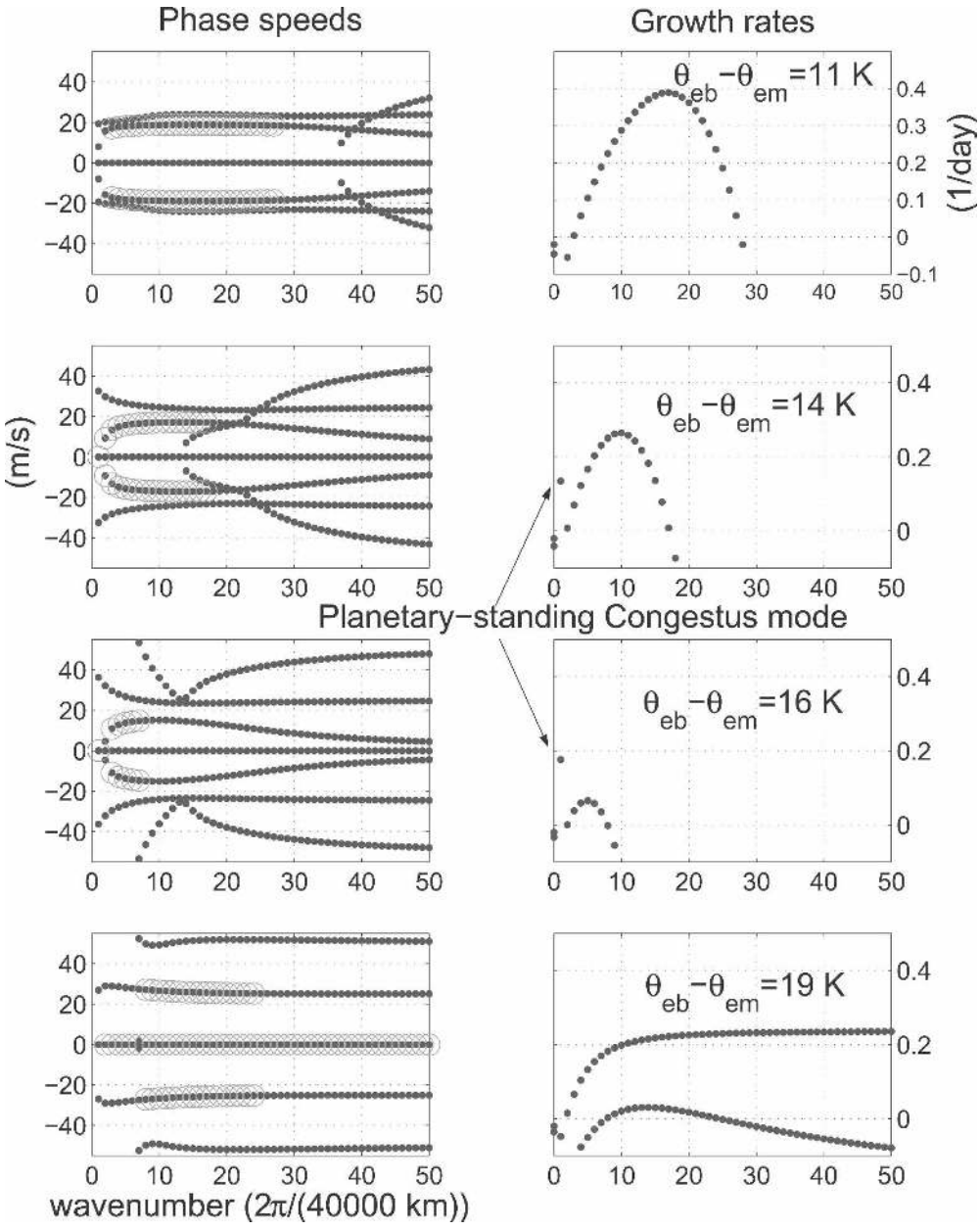

FIG. 2. Linear waves: (left) Phase speeds and (right) growth rates as functions of the zonal wavenumber for different RCEs showing the transition from a deep-convection-dominated regime to a congestus-dominated regime. The unstable modes are highlighted by small circles in the phase plots.

below. We consider three typical wave regimes achieved by the model when the value of $\overline{\theta}_{eb} - \overline{\theta}_{em}$, measuring the moistness/dryness of the troposphere at RCE, is increased, allowing a transition from a deep-convective-dominated regime, with $\overline{\Lambda} \approx \overline{\Lambda}^*$ and $H_c \approx 0$ and $\overline{H}_d \approx \overline{Q}_d$, to a congestus-dominated regime, with $\overline{\Lambda} \approx 1$ and $\overline{H}_c \approx \overline{Q}_c$ and $\overline{H}_d \approx 0$; see (2.8). In Fig. 2, we plot the growth rates and phase speeds as functions of the zonal wavenumber k for values of $\overline{\theta}_{eb} - \overline{\theta}_{em}$ varying from 11 to 19 K. At $\overline{\theta}_{eb} - \overline{\theta}_{em} = 11$ K, we have convectively coupled moist gravity waves (KM06) that are unstable at large and synoptic scales, ($3 \leq k \leq 28$, with phase speeds between 15 and 20 m s^{-1}. The dominant growth rate is about 0.4 day^{-1} and is attained at wavenumber 16, corresponding to a wavelength of about 2500 km. At $\overline{\theta}_{eb} - \overline{\theta}_{em} = 14$ K, the instability of the moist gravity waves weakens and shifts somewhat toward the large scales and a standing mode, unstable at

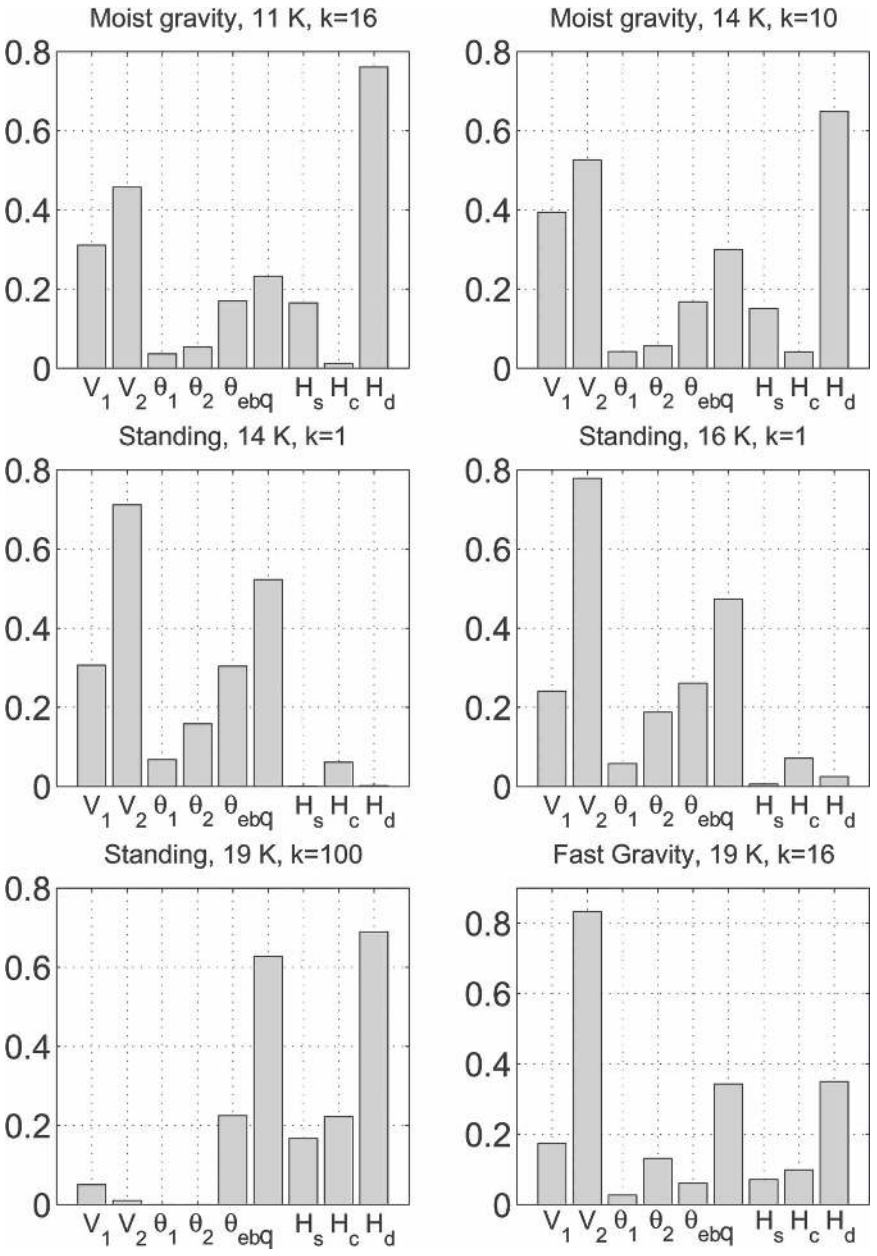

FIG. 3. Bar diagrams showing the projection strengths in the phase space of unstable modes associated with the different RCE regimes in Fig. 2: The wavenumbers for the gravity waves on the top and bottom-right panels correspond to the instabilities peaks.

wavenumber $k = 1$, appears. Interestingly, the growth of the standing mode constitutes an isolated peak completely detached from the smooth curve representing the growth rates of the moist gravity wave branches, which now peaks at around wavenumber $k = 10$. At this parameter value the moist gravity wave growth peak is larger than the growth of this single planetary standing mode but, when $\overline{\theta}_{eb} - \overline{\theta}_{em} = 16$ K, the growth of the planetary standing mode exceeds those of the moist gravity waves. Note that the emergence of the $k = 1$ standing mode is associated solely with the higher congestus heating at RCE corresponding to the larger value of $\overline{\theta}_{eb} - \overline{\theta}_{em}$, that is, $\overline{\Lambda}$. Accordingly, we refer to this mode as the "planetary standing congestus" mode. This distinction is justified by the eigenstructures given in Figs. 3 and 4. Notice that this is distinct from the planetary standing mode reported in Khouider and Majda (2006c), as it is dominated by congestus heating. An-

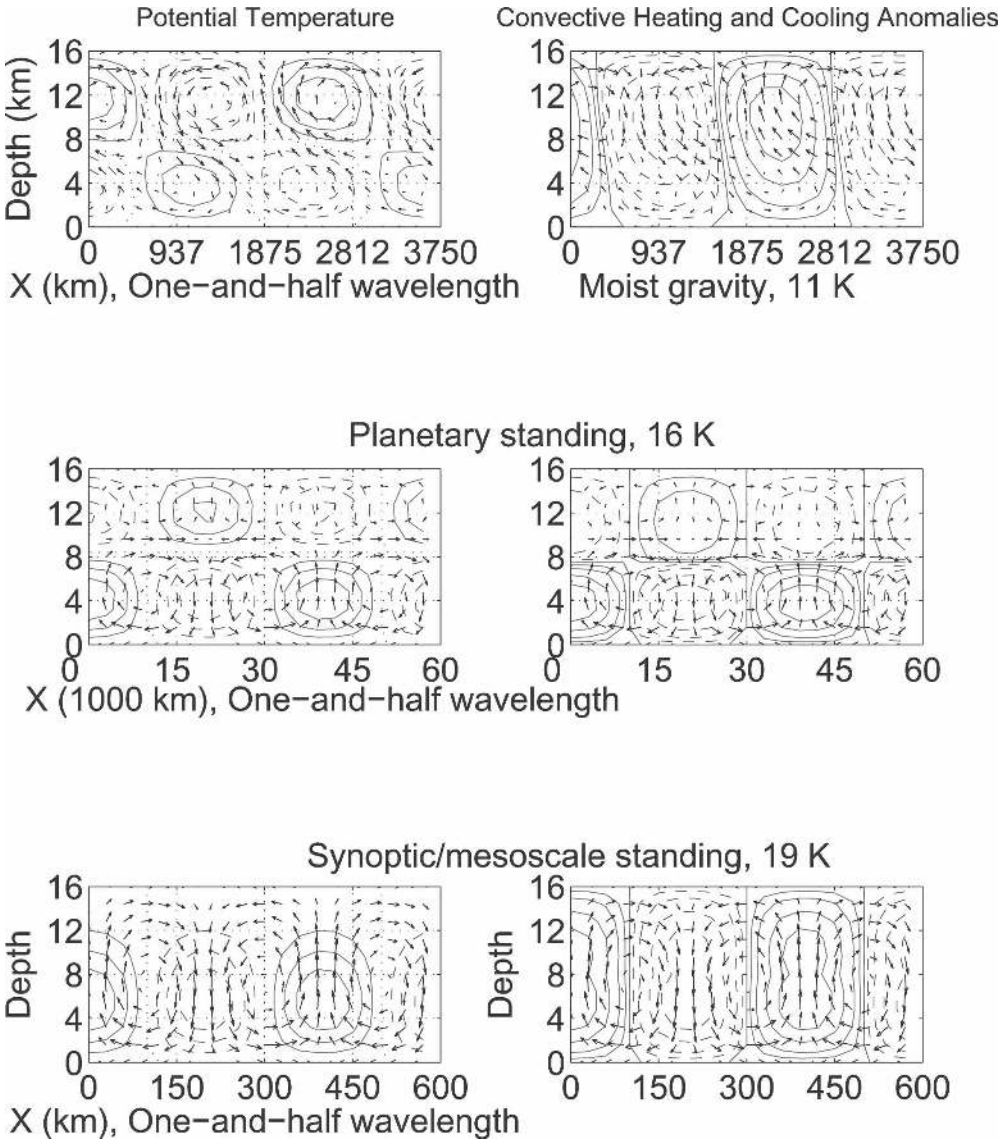

FIG. 4. (top) Potential temperature and convective heating contours of the moist gravity wave associated with the (top) deep convective regime $\overline{\theta}_{eb} - \overline{\theta}_{em} = 11$ K, (middle) the planetary standing mode associated with $\overline{\theta}_{eb} - \overline{\theta}_{em} = 16$ K, and (bottom) the standing mode associated with $\overline{\theta}_{eb} - \overline{\theta}_{em} = 19$ K in the zonal vertical domain. One-and-half zonal wavelengths are shown; the arrows represent velocity profiles.

other transition appears at the extremely dry case when $\overline{\Lambda} \approx 1$. At $\overline{\theta}_{eb} - \overline{\theta}_{em} = 19$ K, the growth and phase diagrams look completely different from the previous ones. They display a standing mode that is unstable at all wavenumbers $k \geq 3$ with growth rates asymptotically approaching a constant value slightly larger than 0.2 day^{-1}. This is reminiscent of the standing mode achieved in the limit $\tilde{\lambda} = 0$ by the original model (KM06). In addition to this standing mode we also have gravity waves moving at about 25 m s^{-1} (the speed of the dry second baroclinic Kelvin waves) that are unstable at synoptic scales between wavenumbers 8 and 24, though with much smaller growth rates.

b. Sensitivity to parameter values

The coarse approximation approach utilized here, for the multicloud models, is somewhat reflected by the large number of parameters in Table 1. As expected, the results reported above are sensitive to some of these parameters. Indeed, many of the parameter values utilized here were selected after an extensive search in the multidimensional parameter domain. (However,

because of page limitation, we cannot report all of the results in detail.) The results reported above constitute the typical statistically significant wave regimes achieved by the model. Here we attempt to summarize briefly the sensitivity of those regimes to variations in parameter values.

Nevertheless, many of the parameters in Table 1, namely, Z_T, h_b, C_d^0, u_0, τ_R, τ_D, τ_s, τ_{conv}, α_s, $\theta_{eb}^* - \overline{\theta}_{eb}$, $Q_{R,1}^0$, $\theta^{\pm}$, $\tilde{Q}$, $\tilde{\lambda}$, and $\tilde{\alpha}$, are climatological parameters that are found in previous idealized convective parameterizations with coarse vertical resolutions (Emanuel 1987; Mapes 1993, 2000; Neelin and Yu 1994; Yano et al. 1995, 1998; Neelin and Zeng 2000; Majda and Shefter 2001a,b; Fuchs and Raymond 2002; Majda and Khouider 2002; Majda et al. 2004; KM06). They are fixed to their standard values, typically derived according to a tropical sounding. Some other parameters, such as m_0, τ_e, and $Q_{R,2}^0$, are determined by the RCE solution based on the given sounding values. The rest of the parameters in Table 1 are characteristic of the multicloud models. It is interesting to notice that changes in some of those parameters, such as a_0, a_1, a_2, and τ_c, only shift the transition between the three wave regimes, reported above, as $\overline{\theta}_{eb} - \overline{\theta}_{em}$ is increased. For instance, large values of a_0 yield smaller growth rates for the moist gravity waves and an earlier transition to the congestus standing mode regime. Notice that this makes sense physically since large a_0 implies a more rapid response of deep convection to variations in $\theta_{1,2}$, and thus leads to less buildup of bulk energy available for deep convection. Similarly, when a_0' is increased, the congestus instability weakens. Also, it is worthwhile noting that when a_0 is large the purely deep convective RCE (no congestus, $\overline{\theta}_{eb} - \overline{\theta}_{em} < 10$ K) is stable, and smaller a_0 values (≤ 4) yield a stable transition between the moist gravity wave and the congestus mode regimes. Moreover, variations in the congestus and stratiform precipitation fractions, f_s and f_c, imply some qualitative changes in the wave structure reported below because of the induced asymmetry in the heating profiles. They do not exhibit significant changes in the stability and phase diagrams except for the standing mode instability at all wavenumbers, which is associated with the extremely dry RCEs (regime 3) that disappears when $f_c = 0$. Finally, notice that the enhanced congestus parameterization requires smaller values of $\mu = 0.25$ and $\alpha_c = 0.1$ compared to the values $\mu = 0.5$ and $\alpha_c = 0.5$ utilized in KM06. Large μ and α_c values yield an instability of the mean state RCE; that is, wavenumber $k = 0$ (KM06).

c. Physical structure of unstable modes

A first look at the eigenmode structure associated with the waves in Fig. 2 is given by the bar diagrams, representing the relative component strengths, plotted in Fig. 3, for each one of the unstable waves at their typical length scales. The two top panels compare the moist gravity waves at their instability peaks associated with the RCE $\overline{\theta}_{eb} - \overline{\theta}_{em} = 11$ K and $\overline{\theta}_{eb} - \overline{\theta}_{em} = 14$ K, respectively. The only apparent discrepancy between the two waves is that the latter has a relatively stronger congestus (H_c) and weaker deep convective (H_d) component. This agrees with the intuition that larger RCE values will allow larger fluctuations, and vice versa. Except for their larger congestus components, the two waves look similar to the usual moist gravity waves reported in KM06. The planetary standing mode diagrams corresponding, respectively, to $\overline{\theta}_{eb} - \overline{\theta}_{em} = 14$ K and $\overline{\theta}_{eb} - \overline{\theta}_{em} = 16$ K are reported on the two middle panels. The most striking feature of this mode is that it has a congestus component much stronger than its deep convective counterpart, which results in stronger u_2 and θ_2 components. On the other hand, the standing mode with an instability band expanding to small scales associated with $\overline{\theta}_{eb} - \overline{\theta}_{em} = 19$ K, shown on the left bottom panel, displays a completely different pattern. It has a significant congestus component, but, somewhat surprisingly, the deep convection is stronger. Notice also that the fluid mechanic variables (u, θ) are much weaker than the moist thermodynamic variables, namely, q and θ_{eb}, suggesting that this mode is thermodynamic in nature, directly coupling the boundary layer and the middle troposphere moisture variables. It resembles the standing mode found in other studies with different convective parameterizations (Fuchs and Raymond 2002; KM06; Khouider and Majda 2006c). Finally, the second baroclinic nature of the synoptic-scale gravity waves moving at about 25 m s^{-1} associated with the case $\overline{\theta}_{eb} - \overline{\theta}_{em} = 19$ K is evident from the strong u_2 and θ_2 components on the bottom right panel.

A more detailed picture of the unstable linear waves is given by the contours of the potential temperature, $\Theta(x, z) \equiv \theta_1 \sin(z) + 2\theta_2 \sin(2z)$ (KM06), and the total convective heating and cooling field,

$$H(x, z) \equiv H_d(x)\Phi_1(z) + H_c(x)[\Phi_2(z) - \delta_c\Phi_2(Z_T - z)] + H_s(x)[\Phi_2(Z_T - z) - \delta_s\Phi_2(z)], \quad (3.1)$$

plotted in Fig. 4, with the total velocity field (U, w) profile overlaid. Here $U = u_1 \cos(z) + u_2 \cos(2z)$ is the total zonal velocity and the vertical velocity w is obtained through the divergence constraint. The eastward-moving moist gravity wave associated with the deep-convection-dominated RCE, $\overline{\theta}_{eb} - \overline{\theta}_{em} = 11$ K, is shown on the top panels. The familiar tilts in temperature and velocity profiles, a return flow behind the

wave, a convergent flow near the surface with a westerly wind within the heating region, and a stratiform wake, etc., reminiscent of the convectively coupled tropical waves are all present here. In fact, these waves are essentially identical to the moist gravity waves reported earlier (KM06) and more details on the physics and dynamical features are found there. The planetary congestus standing mode associated with $\overline{\theta}_{eb} - \overline{\theta}_{em} =$ 16 K is reported in the two middle panels. Note that one direct implication of the nonpropagating nature of the wave is that the velocity and temperature profiles are not tilted at all. Instead, we have opposite-signed circulations tacked on top of each other with rising air associated with warm temperatures, and vice versa. Notice that the dominant congestus heating in Fig. 3 results in a much stronger flow in the lower troposphere. The heating contours on the right panel display the same patterns as the Θ contours on the left. This also results from the standing nature of the wave, which is similar to a flow generated by a standing heat source. Moreover, it is demonstrated by a numerical simulation (section 4b) that this mode plays an important role in creating a preconditioned environment, within its congestus active region spanning half the globe, where moist gravity waves evolve and propagate. The bottom panels in Fig. 4 display the physical structure of the standing mode, unstable at all wavenumbers $k \geq 3$, associated with the RCE $\overline{\theta}_{eb} - \overline{\theta}_{em} = 19$ K. It is shown at the mesoscale corresponding to $k = 100$, though it is self-similar at all scales. Note that the structure of this mode is different from that of the planetary mode in the middle panels. Note that its strong deep convective component in Fig. 3 results in an almost purely first baroclinic structure. Also, as a standing mode it has no tilt. Because of its dominating deep convective heating, this mode is a highly precipitating/drying mode, which therefore may stop the propagation of moist gravity waves. We believe that this is the mode that is responsible for the formation of the "convective barriers" at the edges of the warm pool in the numerical experiment reported in section 4a(2).

4. Nonlinear simulations and congestus preconditioning

In this section we perform numerical simulation for the full nonlinear equations in (2.2)–(2.9). We solve these equations in (x, t) variables on a 40 000-km periodic ring representing the perimeter of the earth at the equator. We use an operator time-splitting strategy where the conservative terms on the left of (2.2) and (2.3) are discretized and solved by a nonoscillatory central scheme while the remaining convective forcing terms are handled by a second-order Runge–Kutta method (Khouider and Majda 2005a,b). The mesh size is 40 km and the time step is 2 min. We consider and compare the two RCE regimes $\overline{\theta}_{eb} - \overline{\theta}_{em} = 14$ K and $\overline{\theta}_{eb} - \overline{\theta}_{em} = 16$ K near the transition from the deep-convective-dominated to the congestus-dominated regimes. Notice that from the linear results in Fig. 2, when $\overline{\theta}_{eb} - \overline{\theta}_{em} = 14$ K, the moist gravity wave growth peak dominates but, when $\overline{\theta}_{eb} - \overline{\theta}_{em} = 16$ K, the growth of the planetary congestus standing mode dominates. The background medium used for the deep convective regime consists of both an aquaplanet with a homogeneous SST and a warm-pool-like forcing with a nonzero SST gradient resulting in a bump in θ^*_{eb} over a region of about 10 000 km. In the congestus-dominated regime we consider only an aquaplanet setup.

a. *Deep-convective-dominated regime* $\overline{\theta}_{eb} - \overline{\theta}_{em} = 14$ *K*

1) INTRASEASONAL WAVE ENVELOPES IN AN AQUAPLANET SETUP

Here Eqs. (2.2)–(2.9) with a homogeneous SST background are solved numerically according to the procedure described above for a period of 200 days, until a statistical steady state is reached (Khouider and Majda 2007). Note that, except for $\overline{\theta}_{eb} - \overline{\theta}_{em}$, all the above parameters are reported in Table 1. In Fig. 5 we show the contours in the space–time domain (Hovmöller diagram) of all dynamical variables over the last 100 days of simulation. Note that, because H_s follows a rapid (3 h) adjustment equation to a fraction of H_d, the contour patterns of H_s and H_d are expected to be almost identical. Streaks of moist gravity waves moving in one direction (to the right) at about 17 m s^{-1} are visible on all panels. They constitute a wave train of six individuals. They have therefore a rough average wavenumber 6, which is slightly smaller than the instability peak wavenumber $k = 10$, predicted by linear theory. Contrary to the physical intuition, this shift in wavenumber is not due to a shift in the basic state as the time-averaged solution (not shown) remains relatively homogeneous and identical to the imposed RCE solution. It is thus due to purely nonlinear effects. The corresponding time period is about 4.5 days, reminiscent of tropical superclusters or convectively coupled Kelvin waves (Wheeler and Kiladis 1999; Wheeler et al. 2000; Straub and Kiladis 2002). Also, particularly evident from the second baroclinic and moisture panels, u_2, θ_2, q, and H_c, on the right, we can see two large-scale wave envelopes moving in the opposite direction (to the left) at about 6 m s^{-1}, corresponding to a time period of about 40 days.

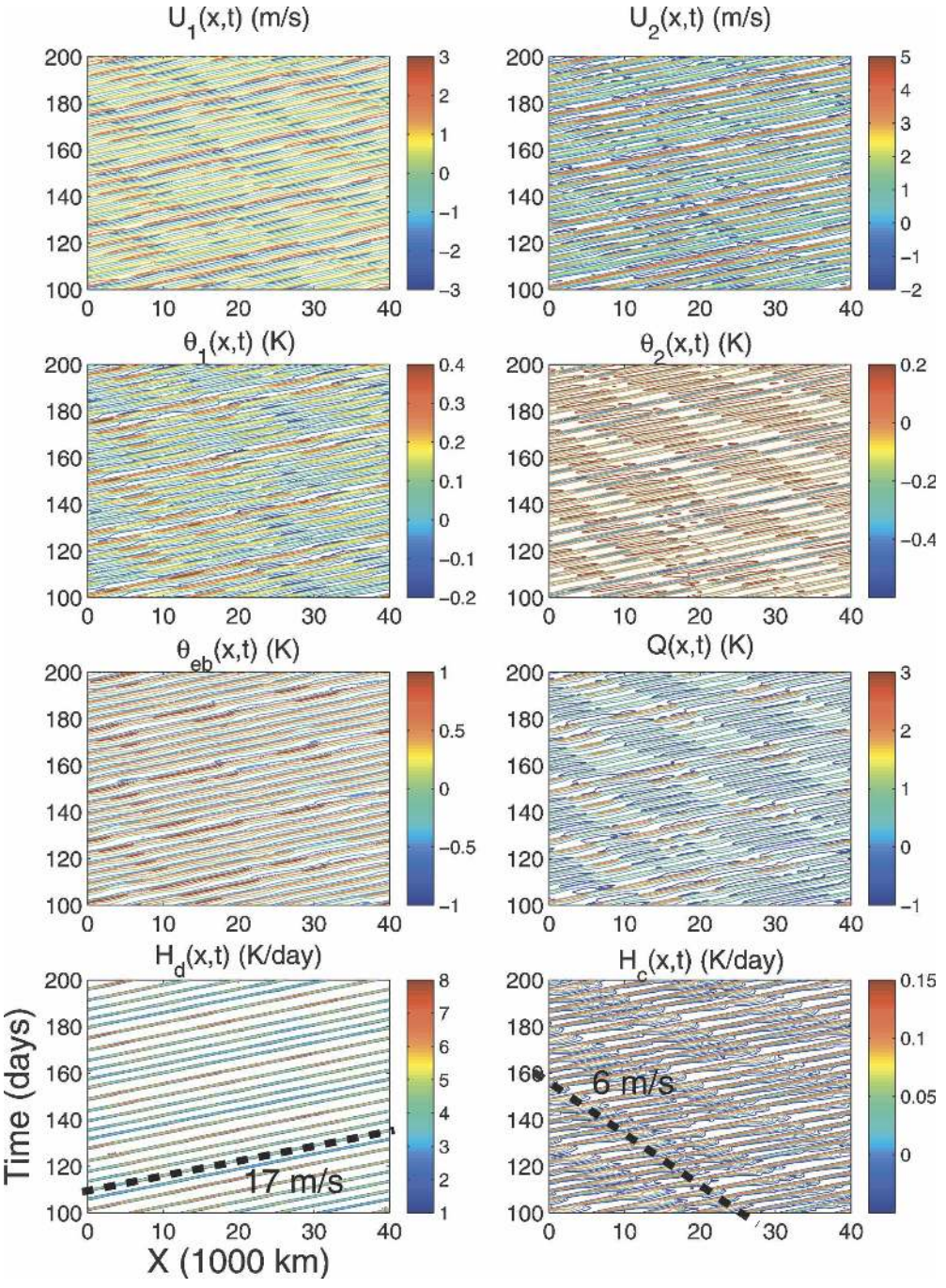

FIG. 5. Plot of x–t contours of the dynamical variables over the last 100 days of simulation: Propagating speeds of 17 m s^{-1} corresponding to the synoptic-scale moist gravity wave packets and of 6 m s^{-1} corresponding to their planetary-scale (wavenumber $k \approx 2$) wave envelopes moving in the opposite direction are shown by the two dashed lines on the two bottom panels, respectively. This is reminiscent of the real world, where the intraseasonal planetary-scale disturbances propagating eastward (the MJO) are modulated by westward synoptic-scale 2-day waves.

Notice that since rotation effects are ignored, there is no preferred direction for wave propagation; gravity waves with similar physical features can move in either direction. In fact, if the x axis on all the panels in Fig. 5 and in Figs. 6 and 7 is reversed so that the planetary wave envelopes move to the "east" while the synoptic-scale moist gravity waves move "westward," then this mimics the eastward propagation of the MJO as an

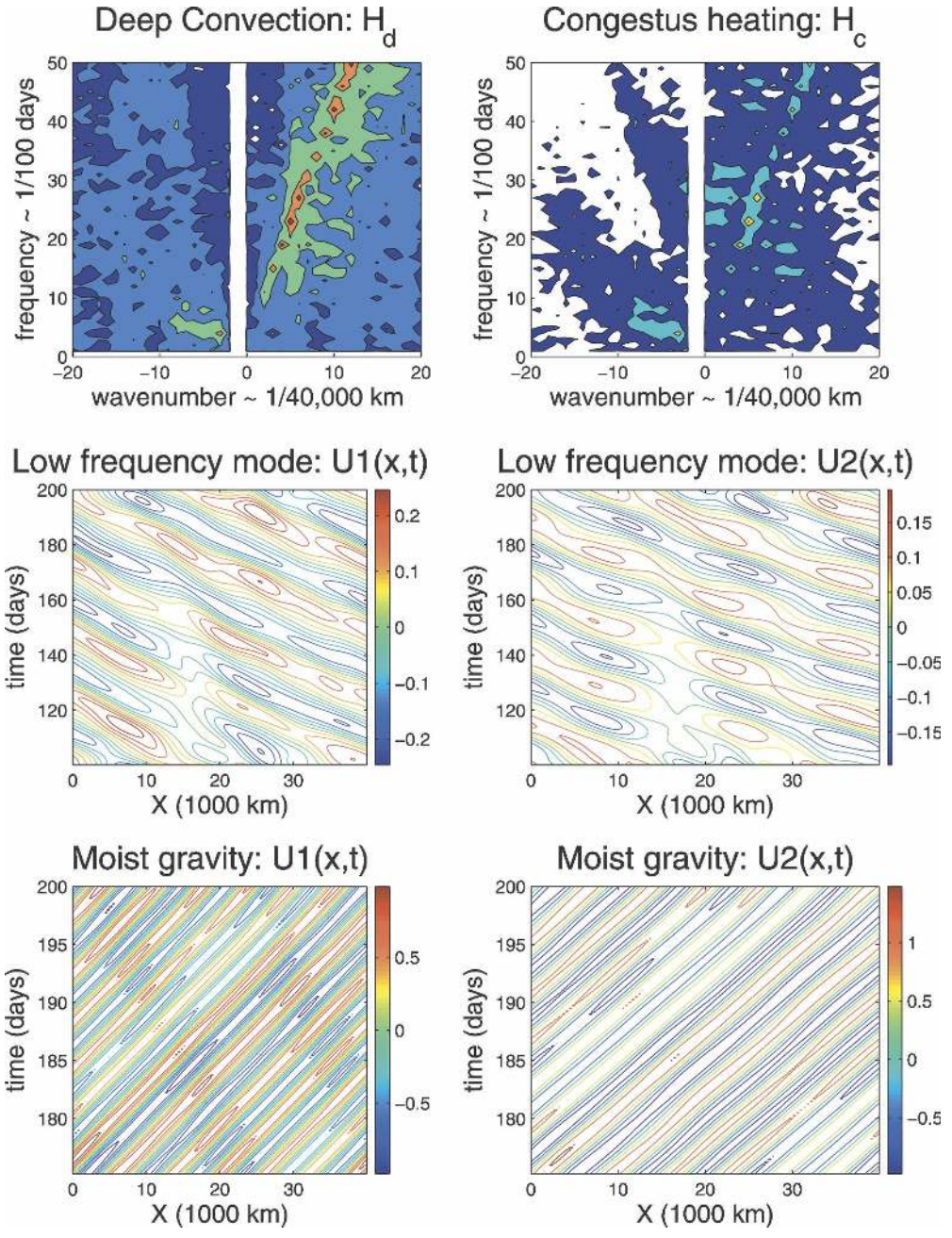

FIG. 6. Log power spectrum of (top) the deep convective and congestus heating rates and (middle) x–t contours of filtered planetary-scale wave envelopes, and (bottom) synoptic-scale moist gravity waves corresponding to the spectral peaks, respectively, on the right and on the left parts of the spectral domain in the top two panels. The first and second baroclinic velocity components are shown.

envelope of westward 2-day waves. However, the latter can be interpreted as a nonlinear envelope of the moist gravity waves predicted by linear theory, moving at the *nonlinear* group velocity of -6 m s^{-1}. We emphasize the nonlinear character of these envelopes because, as the reader can surmise from the corresponding panel on the left of Fig. 2, the group velocity resulting from the linear dispersion relation corresponding to the unstable branch is positive, as the phase speed is positive and nondecreasing for the eastward-moving waves, according to the formula

$$\frac{d}{dk}\left(\frac{\omega}{k}\right) = \frac{1}{k}\left(\frac{d\omega}{dk} - \frac{\omega}{k}\right) \geq 0 \Rightarrow \frac{d\omega}{dk} \geq \frac{\omega}{k} > 0.$$

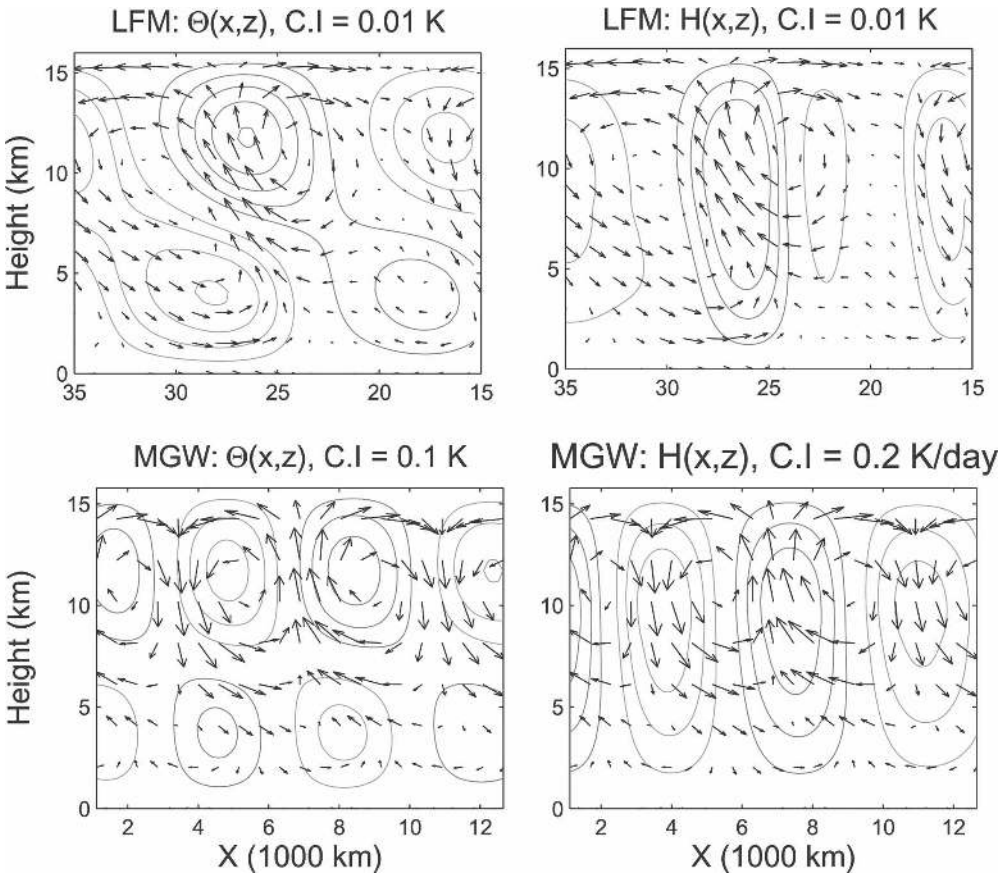

FIG. 7. Zonal and vertical structure of localized time snapshots of (top) the planetary-scale (20 000 km) wave envelope and (bottom) the synoptic-scale moist gravity wave: dark (red) contours are positive and zero contours are not shown; contour intervals (CIs) are indicated in each panel. The arrows represent the (U, W) velocity field. The vertical velocity is amplified by a factor of 500 to account for the aspect ratio; (top) Max $U = 0.26$ m s^{-1}, max $W = 0.06$ cm s^{-1}, and (bottom) max $U = 2.18$ m s^{-1}, max $W = 0.50$ cm s^{-1}. Note that the x axis in the top panels is reversed for a better comparison.

Nevertheless, the mechanisms responsible for the formation and propagation of the nonlinear envelopes are not yet elucidated and are subject to future research.

To confirm the existence and the structure of waves moving in both directions, we plot in the top panels of Fig. 6 the log of the power spectrum of the deep convective and congestus heating rates H_d and H_c. Clearly, the spectral peaks on the left and right correspond, respectively, to the moist gravity wave packets and their low frequency envelopes. Note that there are significant spectral peaks in the moist gravity waves from 4.5 to 2 days, reminiscent of the spectral peaks for both Kelvin waves and 2-day waves (Haertl and Kiladis 2004). These peaks are then used to filter out the left- and the right-moving waves via Fourier space filtering windows where wavenumbers and frequencies outside $-10 \le k \le -1$, $1 \le \omega \le 11$ and $1 \le k \le 11$, $10 \le \omega \le 30$, respectively, are set to zero. Contours of $u_1(x, t)$ and $u_2(x, t)$ for the resulting filtered fields are shown on the middle and bottom panels, respectively. Both wavenumbers (6 and 2) and the periods (4.5 and 40 days) are confirmed from these contour plots. Note that the planetary-scale wave is significantly weaker than the synoptic-scale disturbance, which in turn is weaker but remains comparable to the raw data in Fig. 5.

In Fig. 7, we show the zonal and vertical structure of two localized time snapshots representing each one of the two different wave categories. The low-frequency planetary waves (moving to the left) are represented on the two top panels and the faster synoptic-scale moist gravity wave packets (moving to the right) are represented on the bottom panels. Both (total) potential temperature and (total) heating fields (3.1) are shown. Although they occur on largely different temporal and spatial scales, consistent with the linear wave in Fig. 4, the waves in Fig. 7 share many qualitative features, reminiscent of convectively coupled tropical waves (Wheeler and Kiladis 1999; Wheeler et al. 2000; Straub

and Kiladis 2002; Kiladis et al. 2005; KM06; Khouider and Majda 2006b, 2007). These features include a backward and upward tilt in the wind and temperature fields, upper-tropospheric warm temperature anomalies slightly leading and/or within the region of upward motion, which is in phase with the heating anomalies, low-level convergence and congestus heating leading the wave, and an upper-tropospheric stratiform wake. Nevertheless, the planetary wave envelope has a westerly wind burst near the surface in the middle to rear of the wave, typical of the MJO (Lin and Johnson 1996; Kiladis et al. 2005; Zhang 2005), that dominates the return flow, while the synoptic-scale wave has a middle-tropospheric return flow that is rather symmetric, regarding its westerly and easterly components on each side of the heating region. This difference in morphology is attributed to the combination of the abundance of shallow/congestus) convection ahead of the wave and the strong stratiform cooling in its wake for the intraseasonal/planetary-scale disturbances, as in the real world (Kiladis et al. 2005). The analog of the westerly wind burst and easterly/westerly wind strength, as well as the mean heating in the planetary-scale envelope, are, however, rather weak in comparison with other multiscale MJO models (Biello and Majda 2005; Majda et al. 2007) and actual observations (Zhang 2005). The qualitative self-similarity across scales in the structure of convectively coupled tropical waves is not new and is not restricted to the present model results. In fact, a recent study using multiscale asymptotics (Majda 2007) has provided a theoretical framework for explaining this self-similarity behavior among convectively coupled tropical waves, from mesoscale squall lines to synoptic-scale superclusters to planetary/intraseasonal-scale disturbances, which is widely recognized by the observational experts (G. N. Kiladis 2006, personal communication; Mapes et al. 2006).

2) SST GRADIENT AND EMERGENCE OF CONGESTUS BARRIERS AT THE WARM POOL BOUNDARIES

Now we impose an SST gradient for the background climate so that θ_{eb}^{*} is raised above its spatial mean by up to 5° over a warm pool region of about 10 000 km in extent and lowered by the same amount outside the warm pool, as in Khouider and Majda (2007). Namely, we set

$$\theta_{eb}^{*}(x) = 5\cos\left(\frac{4\pi x}{40\,000}\right) + 10\ \text{K},$$

if $10\,000 \le x \le 30\,000$ km and $\theta_{eb}^{*}(x) = 5$ K elsewhere. All other parameters are kept the same as in 4a(1) except for the integration time, which is now 300 days. In Fig. 8 the x–t contours of the deviations from the time mean of u_1, u_2, H_d, and H_c, averaged over the last 100 days of simulation, are plotted. As the reader can surmise from the contours of u_1 and u_2, there is a lot of wave activity in a region centered within the warm pool and very weak activity outside it. Within the warm pool, we mainly see streaks of convectively coupled waves moving in both directions, at roughly 17 m s^{-1}, that speed up and die as they leave the warm pool region. Outside the warm pool the waves on the u_1 and u_2 panels move at different speeds. In fact, those on the u_1 panel move at about 50 m s^{-1}, while those on the u_2 panel move at 25 m s^{-1}, which are the dry gravity wave speeds associated with the first and second baroclinic modes. A simple look at the heating panels at the bottom confirms that, indeed, these waves are dry and uncoupled since both H_d and H_c vanish right outside the warm pool region from which the moist gravity waves originate. As they enter the dry region outside the warm pool, convectively coupled gravity waves split and project into the first and second free (dry) baroclinic waves and ultimately dissipate and die. Other, weaker, convective waves and convective activity seem to originate far away from the warm pool at the extremities of the domain.

To understand the model mechanisms responsible for this behavior, we plot the zonal structure of the time-averaged fields in Fig. 9. First, note the sharp jumps in all variables at the warm pool boundaries where convection ceases, except for θ_1 and θ_2, which remain continuous; this is actually a good indicator that this is not a numerical artifact. More importantly, notice the sharp peaks in θ_{eb} and H_c and the sudden drop in moisture, q, prior to these peaks. Each of these peaks is resolved and extends over about seven grid points, corresponding roughly to a narrow region of about 250 km. Notice that over this region $\theta_{eb} - \theta_{em}$ exceeds the dry threshold of $\theta^{+} = 20$ K so that $\Lambda = 1$ and $H_d \equiv 0$. These constitute congestus-only regions, surrounding the warm pool, where deep convection is inhibited; this behavior is similar to that hypothesized in Fig. 13 of Johnson et al. (1999). We believe that, in the present setting, this is due to a mode similar to the linear standing mode corresponding to $\overline{\theta}_{eb} - \overline{\theta}_{em} = 19$ from Figs. 3 and 4. The x–z structure of the resulting mean Walker circulation is shown in Fig. 10. Note that both heating and potential temperature mean profiles look different from those reported in Khouider and Majda (2007) with the original multicloud models using a congestus closure based on the downdrafts. The major differences reside in the strong congestus heating and cooling cor-

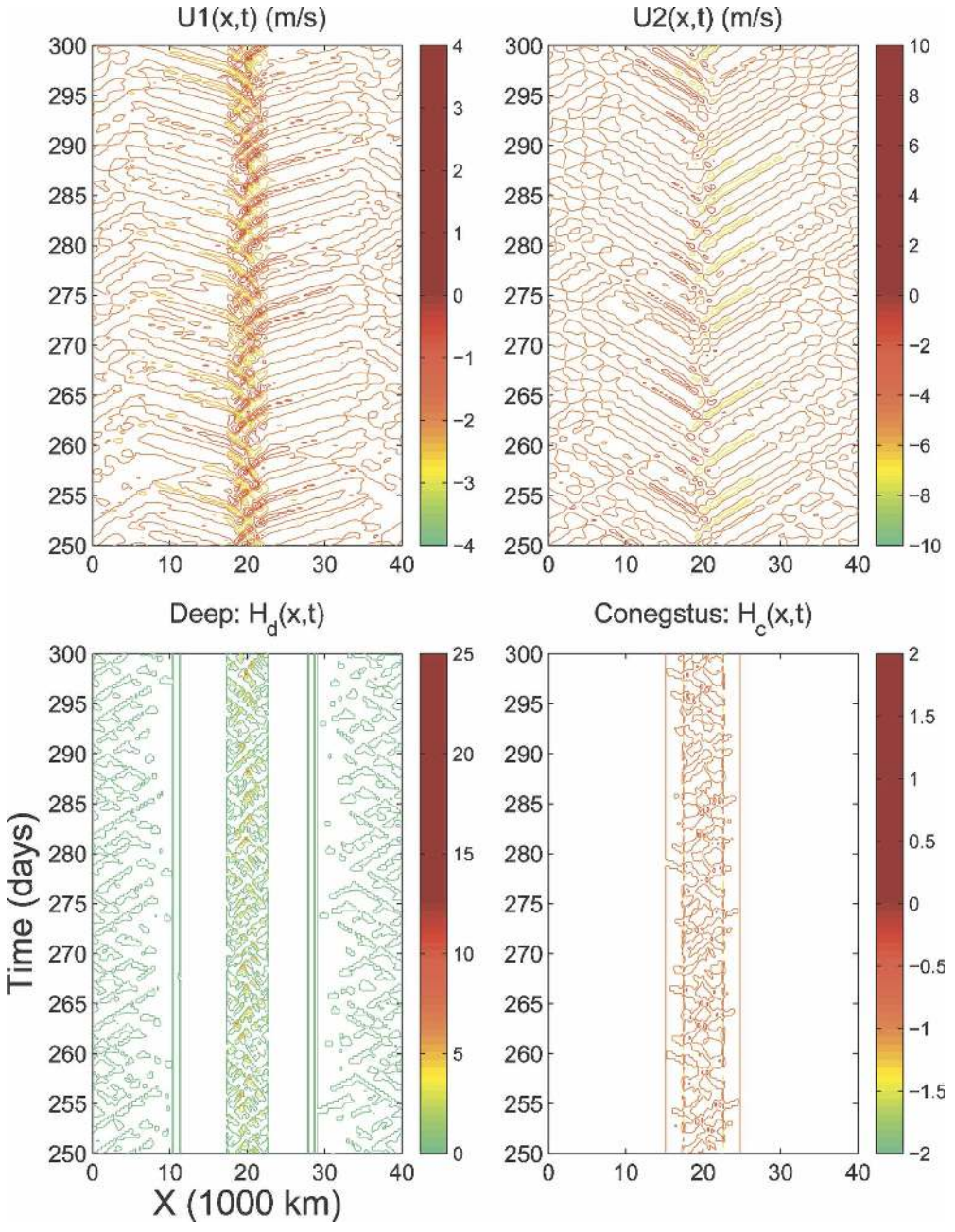

FIG. 8. Contours of deviations from the time-averaged mean of the first and second baroclinic velocity components, $u_1(x, t)$, $u_2(x, t)$, and deep convective and congestus heating rates, $H_d(x, t)$, $H_c(x, t)$, during the last 50 days of simulation for the case with warm pool forcing (see text for details).

responding to the sharp peaks at the warm pool boundaries and the resulting lower-tropospheric warming.

b. Congestus-dominated regime $\overline{\theta}_{eb} - \overline{\theta}_{em} = 16$ K: The congestus preconditioning mode

Here we solve the equations with the same configuration and parameter values as in section 4a(1) except for $\overline{\theta}_{eb} - \overline{\theta}_{em} = 16$ K so that the growth of the congestus standing mode at wavenumber 1 dominates (see Fig. 2). The total integration time is again 300 days. Notice, in particular, that we have an aquaplanet setup with uniform SST. In Fig. 11, we plot the x–t contours of the deviations from the time mean averaged over the last 100 days for u_1, u_2, H_d, and H_c. The most striking feature from these plots is that, for no apparently obvious reason, convective activity and convective waves seem

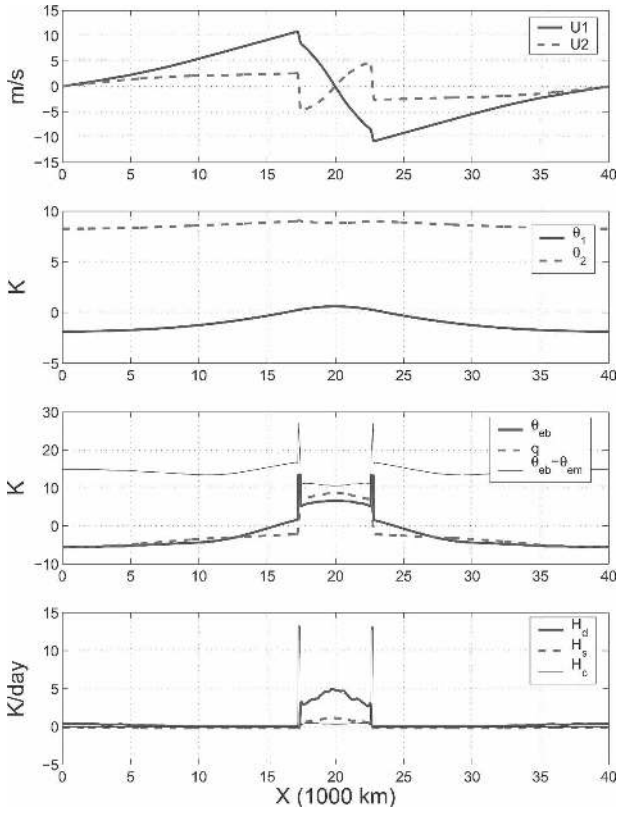

FIG. 9. Zonal structure of the time-averaged flow variables for the case with a warm pool forcing: the average is taking on the last 100 days of simulation. Note that θ_{eb}–θ_{em} exceeds the dry threshold of $\theta^{+} = 20$ K at the congestus barriers.

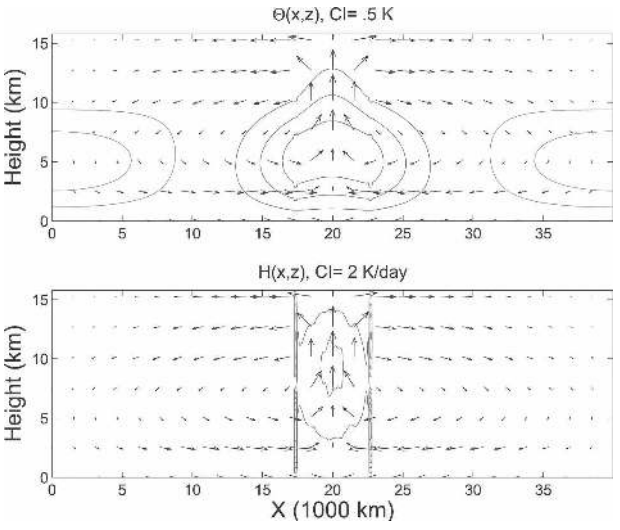

FIG. 10. Zonal vertical structure of the time-averaged mean flow: contours of (top) (total) potential temperature and (bottom) the total heating and cooling are shown with the (U, W) velocity profile overlaid. Max $U = 13$ m s^{-1}, max $W = 16$ cm s^{-1}; W is rescaled by a factor of 500 to account for the aspect ratio. The zonal means were removed from the contoured variables for more clarity. The contour intervals are respectively 0.5 K and 2 K day^{-1}.

to be confined to a region expanding over exactly half of the domain. Moreover, congestus heating is particularly zero outside this region. The only plausible explanation for such behavior comes from the standing congestus mode predicted by linear theory at $\overline{\theta}_{eb} - \overline{\theta}_{em} = 16$ K, which is now active because its growth dominates that of the moist gravity waves. As such it creates a preconditioned region of strong low-level moisture convergence, favorable for deep convection where convectively coupled gravity waves evolve and propagate. A plausible explanation of this congestus preconditioning mechanism through the second baroclinic divergence is obtained from the model equations (2.2), (2.3), and (2.6) and is related directly to the large value of $\tilde{\lambda}$ (see also KM06). Within the congestus-dominated regions we have

$$\frac{\partial \theta_2}{\partial t} - \frac{1}{4}\frac{\partial u_2}{\partial x} \approx H_c > 0 \Rightarrow \frac{\partial q}{\partial t} \approx -\tilde{Q}\tilde{\lambda}\frac{\partial u_2}{\partial x} - \xi_c H_c$$

$$\frac{\partial q}{\partial t} \simeq \left(1 - \frac{\xi_c}{4}\right)\left(-\frac{\partial u_2}{\partial x}\right) > 0 \Rightarrow Q_c > 0.$$

In fact, from the contours of u_1 and H_d in Fig. 11, these waves seem to emanate from outside the congestus active region and amplify as they encounter the preconditioned environment. On the other hand, the waves also seem to suddenly weaken and die as they leave this region. Moreover, as shown in Fig. 12, a nontrivial Walker-like circulation emerges from the time-averaged flow without having to impose a warm pool bump in the background θ^{*}_{eb}, as done in section 4a(2). Note the elevated mean levels of both θ_{eb} and moisture q over the region of convective activity. To the best of the authors' knowledge, such a planetary-scale congestus stationary mode is not (yet!) observed in nature. This result raises the following question about the formation and maintenance of the Indian Ocean/western Pacific warm pool and the related low-frequency processes, such as El Niño: are they solely due to oceanic dynamics or, as occurs here, does the feedback from tropical convection, especially congestus clouds, play a major role in this regard? Such superposition and compensating effects between congestus and deep convective activity within tropical large-scale convective systems are widely observed in nature and have been recognized by many researchers (Kiladis et al. 2005; Mapes et al. 2006).

5. Concluding discussion

Here the basic multicloud models introduced recently by KM06 are generalized to allow asymmetric stratiform and congestus heating and cooling and an

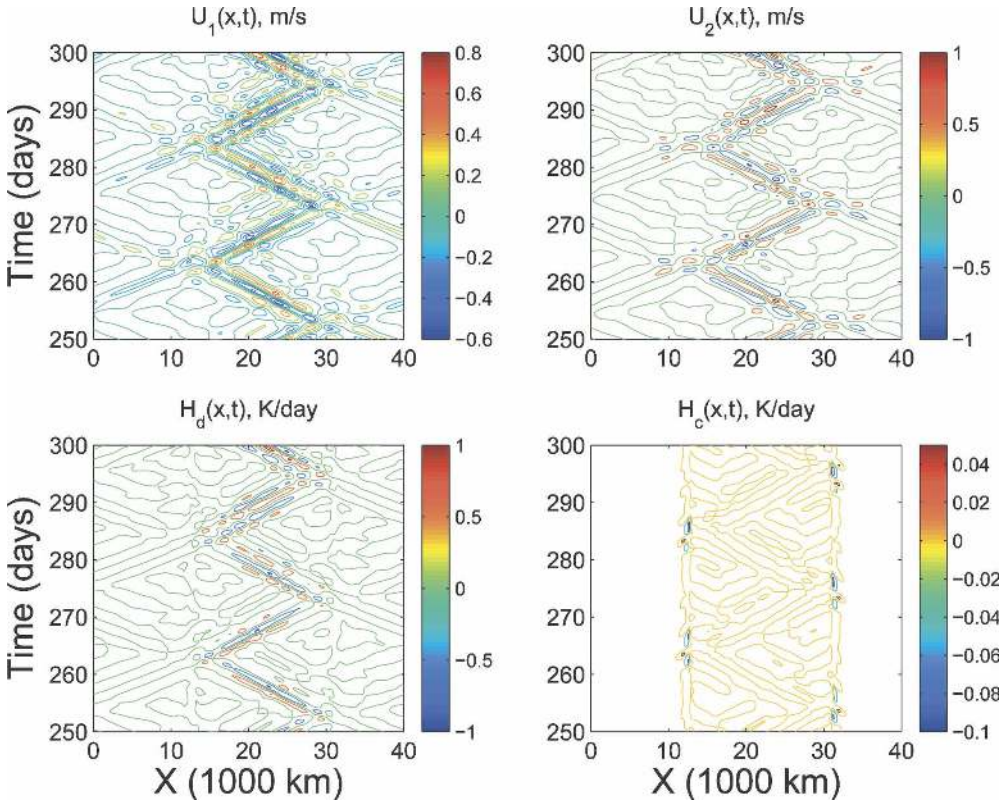

FIG. 11. The x–t contours of u_1, u_2, H_d, and H_c time mean deviations: the case of a congestus-dominated RCE corresponding to $\overline{\theta}_{eb} - \overline{\theta}_{em} = 16$ K with a uniform SST is shown. Convectively coupled waves evolve and propagate within the congestus preconditioned regions.

enhanced congestus parameterization. Linear stability analysis revealed that, in suitable parameter regimes, the new model supports moist gravity waves that are unstable at synoptic scales, with phase speeds and physical structure reminiscent of convectively coupled tropical Kelvin waves, much like those obtained by the original model in KM06, except for the congestus heating that is now stronger, especially for congestus-dominated RCEs. Moreover, a new standing congestus mode, unstable at the planetary wavenumber $k = 1$, emerges for sufficiently dry mean states. The physical structure of this mode is dominated by congestus heating and stronger lower-tropospheric flow and low-level temperature variations. This particularly induces low-level moisture convergence within the congestus active heating, which results in a significant moistening in that region. At $\overline{\theta}_{eb} - \overline{\theta}_{em} = 16$ K, the growth rate of this congestus mode dominates.

The nonlinear simulations, performed and reported in section 4, revealed three interesting findings. First, we consider the deep-convective-dominated RCE, with $\overline{\theta}_{eb} - \overline{\theta}_{em} = 14$ K, in an aquaplanet setup without rotation and without meridional dependence. As one would expect, moist gravity wave packets similar to those predicted by the linear theory emerge. They have a phase speed of about 17 m s^{-1} and a zonal wavelength from 6000 to 7000 km. Apparent from both the raw data contours in Fig. 5 and the power spectra and filtered fields in Fig. 6, these wave packets have planetary-scale wave envelopes moving at about 6 m s^{-1} in the opposite direction. The physical structures plotted in Fig. 7 revealed that both synoptic-scale wave packets and their low-frequency envelopes have many of the self-similar physical and dynamical features of convectively coupled waves, reminiscent of the fashion in which tropical superclusters and two-day waves modulate the Madden–Julian oscillation (Wheeler and Kiladis 1999; Wheeler et al. 2000; Straub and Kiladis 2002; Haertl and Kiladis 2004; Kiladis et al. 2005). These simulations in the present context confirm the self-similarity across scales in the structure of convectively coupled tropical waves, from mesoscale squall lines to synoptic-scale superclusters and two-day waves to planetary/intraseasonal-scale disturbances (G. N. Kiladis 2006, personal communication; Mapes et al. 2006; Majda 2007).

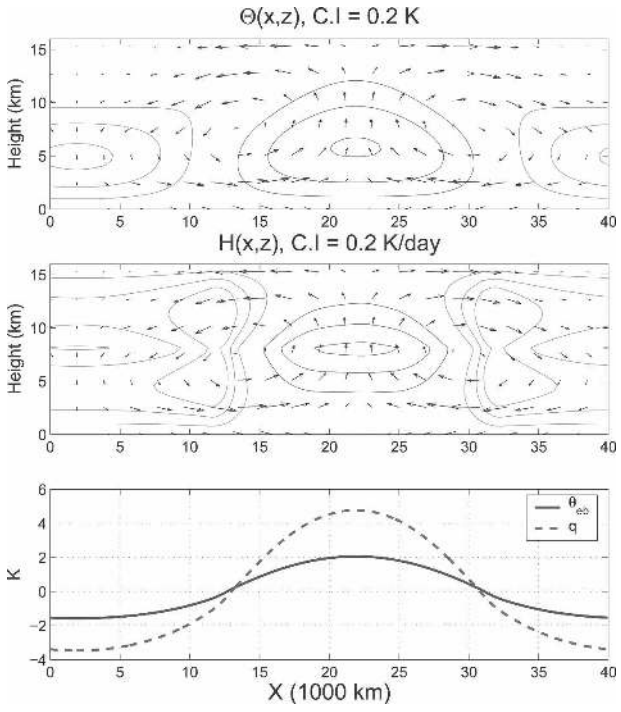

FIG. 12. Time-averaged flow and emergence of a Walker circulation from a uniform SST background: (top) the x–z structure of the mean flow and (bottom) the zonal structure of the mean θ_{eb} and mean q are plotted.

When a warm pool forcing is imposed through a suitable SST gradient, dry regions of roughly 250 km in extent form "convective barriers" surrounding the warm pool region where only congestus heating survives. Deep convection and moist gravity waves emanating within the warm pool region are suppressed when they hit the convective barrier and become dry (free) waves projecting onto first and second baroclinic gravity waves: the only waves supported by the model equations when the convective forcing and coupling are absent. The dry regions surrounding the warm pool constitute congestus-only regions where deep convection is inhibited; this has been hypothesized in Fig. 13 of Johnson et al. (1999).

Finally, it is found that during a nonlinear simulation with an aquaplanet setup in the case with $\overline{\theta}_{eb} - \overline{\theta}_{em} = 16$, the dominating planetary standing congestus mode preconditions and moistens the environment within its congestus active region where moist gravity waves evolve and propagate. This, in particular, results in a Walker-like circulation with raised levels of moisture q and θ_{eb} over the region of deep convection under a uniform SST background. Although, such a planetary-scale congestus stationary mode is not (yet!) observed in nature, this result in the present model raises a question about the Indian Ocean/western Pacific warm pool regarding the significant role of congestus clouds in its maintenance in addition to ocean dynamics. The phenomenon discussed in Figs. 8–12 provide new examples for the propagation and reflection of precipitation fronts in moisture models (Frierson et al. 2004; Khouider and Majda 2005b; Pauluis et al. 2007, manuscript submitted to *Quart. J. Roy. Meteor. Soc.*). The study in the present paper is being extended to the case with rotation and meridional dependence and will be reported elsewhere by the authors in the near future.

Acknowledgments. The research of BK is supported by a grant from the Natural Sciences and Engineering Research Council of Canada. The research of AM is partially supported by ONR N0014-05-1-0164 and NSF DMS-0456713. Insightful comments from the three anonymous reviewers helped improve the text considerably.

REFERENCES

Biello, J., and A. J. Majda, 2005: A new multiscale model for the Madden–Julian oscillation. *J. Atmos. Sci.,* **62,** 1694–1721.

Dunkerton, T. J., and F. X. Crum, 1995: Eastward propagating 2- to 15-day equatorial convection and its relation to the tropical intraseasonal oscillation. *J. Geophys. Res.,* **100,** 25 781–25 790.

Emanuel, K. A., 1987: An air–sea interaction model of intraseasonal oscillations in the tropics. *J. Atmos. Sci.,* **44,** 2324–2340.

——, and D. J. Raymond, 1993: *The Representation of Cumulus Convection in Numerical Models*. *Meteor. Monogr.,* No. 46, Amer. Meteor. Soc., 246 pp.

Frierson, D. M. W., A. J. Majda, and O. M. Pauluis, 2004: Large scale dynamics of precipitation fronts in the tropical atmosphere: A novel relaxation limit. *Commun. Math. Sci.,* **2,** 591–626.

Fuchs, Z., and D. Raymond, 2002: Large-scale modes of a nonrotating atmosphere with water vapor and cloud-radiation feedbacks. *J. Atmos. Sci.,* **59,** 1669–1679.

Haertl, P. T., and G. N. Kiladis, 2004: Dynamics of 2-day equatorial waves. *J. Atmos. Sci.,* **61,** 2707–2721.

Hendon, H. H., and B. Liebmann, 1994: Organization of convection within the Madden–Julian oscillation. *J. Geophys. Res.,* **99,** 8073–8084.

Johnson, R. H., T. M. Rickenbach, S. A. Rutledge, P. E. Ciesielski, and W. H. Schubert, 1999: Trimodal characteristics of tropical convection. *J. Climate,* **12,** 2397–2407.

Khouider, B., and A. J. Majda, 2005a: A non-oscillatory balanced scheme for an idealized tropical climate model. Part I: Algorithm and validation. *Theor. Comput. Fluid Dyn.,* **19,** 331–354.

——, and ——, 2005b: A non-oscillatory balanced scheme for an idealized tropical climate model. Part II: Nonlinear coupling and moisture effects. *Theor. Comput. Fluid Dyn.,* **19,** 355–375.

——, and ——, 2006a: A simple multicloud parameterization for convectively coupled tropical waves. Part I: Linear analysis. *J. Atmos. Sci.,* **63,** 1308–1323.

——, and ——, 2006b: Model multicloud parameterizations for

convectively coupled waves: Detailed nonlinear wave evolution. *Dyn. Atmos. Oceans,* **42,** 59–80.

——, and ——, 2006c: Multicloud convective parameterizations with crude vertical structure. *Theor. Comput. Fluid Dyn.,* **20,** 351–375.

——, and ——, 2007: A simple multicloud parameterization for convectively coupled tropical waves. Part II: Nonlinear simulations. *J. Atmos. Sci.,* **64,** 381–400.

Kiladis, G. N., K. H. Straub, and P. T. Haertl, 2005: Zonal and vertical structure of the Madden–Julian oscillation. *J. Atmos. Sci.,* **62,** 2790–2809.

Lau, W. K. M., and D. E. Waliser, Eds., 2005: *Intraseasonal Variability in the Atmosphere-Ocean Climate System.* Springer-Verlag, 436 pp.

Lin, J.-L., and Coauthors, 2006: Tropical intraseasonal variability in 14 IPCC AR4 climate models. Part I: Convective signals. *J. Climate,* **19,** 2665–2690.

Lin, X., and R. H. Johnson, 1996: Kinematic and thermodynamic characteristics of the flow over the western Pacific warm pool during TOGA COARE. *J. Atmos. Sci.,* **53,** 695–715.

Majda, A. J., 2007: New multiscale models and self-similarity in tropical convection. *J. Atmos. Sci.,* **64,** 1393–1404.

——, and M. Shefter, 2001a: Waves and instabilities for model tropical convective parameterizations. *J. Atmos. Sci.,* **58,** 896–914.

——, and ——, 2001b: Models for stratiform instability and convectively coupled waves. *J. Atmos. Sci.,* **58,** 1567–1584.

——, and B. Khouider, 2002: Stochastic and mesoscopic models for tropical convection. *Proc. Natl. Acad. Sci. USA,* **99,** 1123–1128.

——, and J. Biello, 2004: A multiscale model for the intraseasonal oscillation. *Proc. Natl. Acad. Sci. USA,* **101,** 4736–4741.

——, B. Khouider, G. N. Kiladis, K. H. Straub, and M. G. Shefter, 2004: A model for convectively coupled tropical waves: Nonlinearity, rotation, and comparison with observations. *J. Atmos. Sci.,* **61,** 2188–2205.

——, S. N. Stechmann, and B. Khouider, 2007: Madden–Julian Oscillation analog and intraseasonal variability in a multicloud model above the equator. *Proc. Natl. Acad. Sci. USA,* **104,** 9919–9924.

Mapes, B. E., 1993: Gregarious tropical convection. *J. Atmos. Sci.,* **50,** 2026–2037.

——, 2000: Convective inhibition, subgrid-scale triggering energy, and stratiform instability in a toy tropical wave model. *J. Atmos. Sci.,* **57,** 1515–1535.

——, S. Tulich, J. Lin, and P. Zuidema, 2006: The mesoscale convection life cycle: Building block or prototype for large-scale tropical waves? *Dyn. Atmos. Oceans,* **42,** 3–29.

Moncrieff, M. W., and E. Klinker, 1997: Organized convective systems in the tropical western Pacific as a process in general circulation models: A TOGA COARE case-study. *Quart. J. Roy. Meteor. Soc.,* **123,** 805–827.

Nakazawa, T., 1988: Tropical super clusters within intraseasonal variations over the western Pacific. *J. Meteor. Soc. Japan,* **66,** 823–839.

Neelin, J. D., and J. Yu, 1994: Modes of tropical variability under convective adjustment and Madden–Julian oscillation. Part I: Analytical theory. *J. Atmos. Sci.,* **51,** 1876–1894.

——, and N. Zeng, 2000: A quasi-equilibrium tropical circulation model—Formulation. *J. Atmos. Sci.,* **57,** 1741–1766.

Raymond, D. J., 2001: A new model for the Madden–Julian oscillation. *J. Atmos. Sci.,* **58,** 2807–2819.

Scinocca, J. F., and N. A. McFarlane, 2004: The variability of modeled tropical precipitation. *J. Atmos. Sci.,* **61,** 1993–2015.

Slingo, J. M., and Coauthors, 1996: Intraseasonal oscillations in 15 atmospheric general circulation models: Results from an AMIP diagnostic subproject. *Climate Dyn.,* **12,** 325–357.

Smith, R. K., Ed., 1997. *The Physics and Parameterization of Moist Atmospheric Convection.* Kluwer Academic, 498 pp.

Straub, K. H., and G. N. Kiladis, 2002: Observations of a convectively coupled Kelvin wave in the eastern Pacific ITCZ. *J. Atmos. Sci.,* **59,** 30–53.

Wheeler, M., and G. N. Kiladis, 1999: Convectively coupled equatorial waves: Analysis of clouds and temperature in the wavenumber–frequency domain. *J. Atmos. Sci.,* **56,** 374–399.

——, ——, and P. J. Webster, 2000: Large-scale dynamical fields associated with convectively coupled equatorial waves. *J. Atmos. Sci.,* **57,** 613–640.

Yano, J.-I., J. C. McWilliams, M. W. Moncrieff, and K. A. Emanuel, 1995: Hierarchical tropical cloud systems in an analog shallow-water model. *J. Atmos. Sci.,* **52,** 1723–1742.

——, M. W. Moncrieff, and J. C. McWilliams, 1998: Linear stability and single-column analyses of several cumulus parameterization categories in a shallow-water model. *Quart. J. Roy. Meteor. Soc.,* **124,** 983–1005.

Zhang, C., 2005: Madden–Julian Oscillation. *Rev. Geophys.,* **43,** RG2003, doi:10.1029/2004RG000158.